Al-Cu-Ce(-Zr) alloys with an exceptional combination of additive processability and mechanical properties

Sumit Bahl[1*], Kevin Sisco[2], Ying Yang[1], Felix Theska[3], Sophie Primig[3], Lawrence F. Allard[1], Richard A. Michi[1], Christopher Fancher[1], Benjamin Stump[1], Ryan Dehoff[4], Amit Shyam[1], Alex Plotkowski[1]

[1]Materials Science & Technology Division, Oak Ridge National Laboratory, Oak Ridge, TN 37830, USA

[2]Mechanical, Aerospace and Biomedical Engineering, University of Tennessee, Knoxville, TN, 37996, USA

[3]School of Materials Science & Engineering, UNSW Sydney, NSW 2052, Australia

[4]Manufacturing Science Division, Oak Ridge National Laboratory, Oak Ridge, TN 37830, USA

*Corresponding author. Email: bahls@ornl.gov

Abstract

High-temperature Al-9Cu-6Ce and Al-9Cu-6Ce-1Zr (wt%) alloys were designed for fabrication with laser powder bed fusion additive manufacturing (AM). An ultra-fine eutectic structure comprising FCC-Al and particles of a previously unidentified Al_8Cu_3Ce intermetallic phase was obtained with an inter-particle spacing of approximately 280 nm. The inherent hot-tearing resistance of the eutectic alloys resulted in > 99.5% relative density. A thermodynamic model suggested improved hot-tearing resistance of the present alloys relative to the benchmark AM AlSi10Mg alloy. The Al-Cu-Ce alloy exhibited superior thermal stability with approximately 75% of the as-fabricated hardness retained after 200 h exposure at 400 °C, owed to the coarsening resistance of the intermetallic particles. The Al-Cu-Ce-Zr alloy age-hardened through precipitation of nanoscale Al_3Zr precipitates. The aged microstructure was stable at 350 °C with a 13% higher hardness after 200 h exposure compared to the as-fabricated condition. The combined influence of ultra-fine spacing and coarsening resistance of the intermetallic particles resulted in the higher yield strength of the Al-Cu-Ce and Al-Cu-Ce-Zr alloys compared to AM AlSi10Mg and Scalmalloy at temperatures greater than 200 °C. This work essentially demonstrates that thermally stable Al alloys with exceptional mechanical properties can be produced by additive manufacturing.

Keywords: Al alloys; Eutectic alloys; Additive manufacturing; Laser powder bed fusion; High-temperature; Tensile properties.

1. Introduction

Additive manufacturing (AM) has recently emerged as a powerful tool to manufacture components with complex geometries [1, 2]. Aluminum alloys are widely used in weight-critical structural applications owing to their high specific strength, stiffness, and corrosion resistance [3]. Al alloys with high strength at elevated temperatures have the potential to replace heavier Ti- and Fe- based alloys in aerospace and automotive applications [4]. The non-equilibrium conditions in AM can produce novel alloy microstructures with improved mechanical properties that are difficult to achieve via conventional materials processing routes. The research in AM Al alloys has been largely focused on near-eutectic AlSi10Mg alloy due to its favorable processability [4-10]. The narrow freezing range of AlSi10Mg improves the hot-tearing resistance that makes the alloy processable. Several conventional high-strength wrought Al alloys including 2xxx, 6xxx, and 7xxx series alloys have also been fabricated with AM. The issue of hot-tearing posed a challenge in processing of these alloys but has been mitigated since then through the use of grain refiners [11-21] or alloy modification [22-24]. However, AlSi10Mg and wrought Al alloys are not suitable for use at temperatures above 200 °C due to loss of strength caused by coarsening of the precipitates. An opportunity exists to develop entirely new high-temperature Al alloys that are not only processable with AM but truly leverage the AM processing conditions to achieve exceptional mechanical properties.

Al-Ce is a eutectic system that has recently gained interest particularly for high-temperature applications [25-34]. Similar to AlSi10Mg, near-eutectic Al-Ce based alloys can be suitable for AM processing owing to the narrow freezing ranges. The negligible solid-solubility of Ce in FCC-Al confers superior coarsening resistance to the Ce-rich intermetallic particles in the eutectic structure at elevated temperatures. Czerwinski [35] reported that $Al_{11}Ce_3$ particles in binary Al-Ce

alloys displayed high coarsening resistance at 500 °C, which resulted in the alloys retaining an exceptionally high level of 80% as-cast hardness after 168 h of thermal exposure. The cast Al-Ce based alloys, however, lack strength due to the coarse size and distribution of the intermetallic particles [35]. Plotkowski *et al.* [29] showed that rapid solidification in AM can refine the eutectic structure and increase the strength of Al-Ce based alloys while maintaining thermal stability. The strength of these alloys can be further improved by alloying elements that provide solid-solution and precipitation strengthening. We recently fabricated an Al-Ce-Mn alloy with laser powder bed fusion (LPBF) process that retained 80% of the as-fabricated yield strength after 200 h of exposure at 400 °C [30]. Further, the alloy exhibited 55 MPa yield strength at 400 °C, outperforming a wrought 2618 high-temperature Al-Cu alloy with 30 MPa yield strength at 370 °C. Sisco *et al.* [36] reported that the mechanical properties of a near-eutectic Al-Ce-Mg alloy exceeded that of AlSi10Mg in the room-temperature (R.T.) to 400 °C temperature range. Manca *et al.* [37] reported an AM Al-Cu-Ce alloy with 160 MPa yield strength at 250 °C higher than 130 MPa yield strength of AlSi10Mg at the same temperature [38]. Although existing Al-Ce based alloys have shown promising results, they suffer from certain limitations. The Al-Ce-Mn [30] and Al-Ce-Cu [37] alloys exhibited poor ductility at R.T. The processing of Al-Ce-Mg alloys is difficult due to issues related to vaporization of Mg [36]. Thus, there is a need to continue the development of Al-Ce alloys that are processable and offer a good combination of mechanical properties.

Zr is an important alloying element in AM Al alloys from the standpoint of processability and mechanical properties. It is a grain refiner that has mitigated the problem of hot-tearing in certain AM Al alloys [12-17, 21]. AM Al-Mg alloys modified with Zr develop a bimodal grain size distribution with equiaxed grains near melt pool boundaries and columnar grains away from the boundaries. Such a bimodal grain size distribution has been reported to synergistically improve

the strength and ductility of the alloy at R.T. [39, 40]. The precipitation of nanoscale $L1_2$ Al_3Zr upon aging can improve tensile strength and creep resistance of the alloy [41]. Rapid solidification in AM enhances Zr supersaturation in FCC-Al matrix. The increased amount of Zr is available for precipitation during aging treatment which leads to higher volume fraction of nanoscale Al_3Zr precipitates. [13, 14].

The above discussion highlights two alloy design strategies for AM of Al alloys. One strategy is to design eutectic alloys with a refined structure produced by high solidification rates during AM. The other strategy is to use Zr as a grain refiner and precipitation strengthener in Al alloys. Here, we combined the advantages of a refined eutectic structure and Zr addition to produce new high-performance Al-Ce based alloys. Near-eutectic ternary Al-9Cu-6Ce and quaternary Al-9Cu-6Ce-1Zr (wt%) alloys were produced with LPBF additive manufacturing in this work. The Cu content in the alloy was based on prior work that demonstrated high hot-tearing resistance in Al-Cu alloys at 9 wt% Cu [42, 43]. The 6 wt% Ce is hypo-eutectic in binary Al-Ce system with the eutectic point at 10 wt% Ce and was selected as such to control the fraction of brittle intermetallic phases [29]. The maximum solid-solubility of Zr in FCC-Al is 0.28 wt% in binary Al-Zr alloy [41]. A high Zr content of 1 wt% was added to the alloy considering enhanced supersaturation under rapid solidification conditions present in AM. The alloy microstructures in as-fabricated and heat-treated conditions were characterized with scanning electron microscopy (SEM), electron backscatter diffraction (EBSD), scanning transmission electron microscopy (STEM), atom probe tomography (APT), and synchrotron x-ray diffraction (XRD). The mechanical properties were characterized with hardness and tensile tests. A thermodynamic model was developed to examine the solidification mode and hot-tearing resistance of the alloys. Theoretical models were applied to analyze the strengthening mechanisms. It is demonstrated that rapid solidification in AM can be

leveraged to produce thermally stable bulk eutectic alloys with refined microstructure and exceptional mechanical properties at elevated homologous temperature.

2. Materials and methods

2.1. Manufacturing

Ingots of nominal composition Al-9Cu-6Ce and Al-9Cu-6Ce-1Zr (wt%) were cast by Eck Industries, and powder was Nitrogen gas atomized by Connecticut Engineering Associates Corporation. Volunteer Aerospace Inc. fabricated test samples using a Concept Laser LPBF system. An extensive design of experiments was performed for each alloy to determine process conditions that resulted in high density samples. A total of 49 parameter sets with different combinations of laser power, speed, spot size, hatch spacing, and scanning strategy were tested separately for each alloy. The optimized process conditions as reported in our earlier investigation are summarized in Table 1 [44]. A bidirectional laser scanning strategy was used with 67° rotation in scanning direction for every new layer. Cylindrical samples of 115 mm length and 15 mm diameter were built vertically in Nitrogen atmosphere, and a preheated build plate temperature of 200 °C was applied in all cases to minimize residual stress. Relative density of the as-fabricated alloys determined using optical microscopy was > 99.5%. Additional details on processing of the alloys are given in supplementary information. The chemistry of the as-fabricated samples was measured using inductively coupled plasma – optical emission spectroscopy. The measured compositions are summarized in Table 2 [44]. The as-fabricated alloys were subjected to heat treatments at 250, 300, 350, and 400 °C for times 1, 8, 24, 48, 96, and 200 h.

Table 1 Processing parameters used for each alloy [44].

Parameter	Al-Cu-Ce	Al-Cu-Ce-Zr
Laser power (W)	300	370

Laser speed (mm/s)	1300	2000
Laser spot size (μm)	95	110
Hatch spacing (mm)	0.15	0.1
Layer thickness (μm)	30	30

Table 2 Measured compositions of the as-fabricated alloys, given in wt% [44].

Elements	Al-Cu-Ce	Al-Cu-Ce-Zr
Al	87.20	85.41
Ce	4.73	5.56
Cu	7.78	7.92
Zr	-	0.82
Si	0.07	0.05
Fe	0.11	0.09

2.2. Microstructural characterization

Microstructures were characterized using SEM (S4800 Hitachi) and EBSD (Tescan Mira 3 equipped with a detector form EDAX) at 10 kV and 25 kV accelerating voltages, respectively. Final polishing of samples for SEM and EBSD was performed with colloidal silica solution. EBSD measurements were made at a step size of 0.5 μm. The spacing between intermetallic particles and widths of grains were measured from SEM images and EBSD orientation maps, respectively, using linear intercept method. The lines for intercept measurement were drawn perpendicular to the build direction in the images. Microstructure was also characterized with STEM (JEOL 2200FS) fitted with a CEOS GmbH (Heidelberg, Ger.) aberration corrector and operated at 200kV. Electron transparent STEM foils of 3 mm diameter were prepared by dual-jet electropolishing (Struers A/S TenuPol) with an electrolyte of composition 25% HNO_3 – 75% methanol chilled to -13 °C.

Microstructure was also characterized with APT. Blanks in the dimensions of 0.5 × 0.5 × 2.0 mm^3 were cut using a Struers Minitom with a water-cooled diamond blade. Atom probe tips were electropolished using standard two-step techniques with 25% and 2% perchloric acid between 23 to 11 V [45]. Immediately after electropolishing, batches of up to five tips were transferred into a SEM to verify whether the tip apex was located near or away from a melt pool boundary. A Zeiss Sigma Ultra with 5 kV acceleration voltage, high-current mode, and HD backscattered detector was used to identify the location based on the intermetallic morphology (coarser near melt pool boundary, finer away from melt pool boundary). All atom probe experiments used a Cameca LEAP 3000 with voltage pulsing at 30 K specimen temperature, 200 kHz pulse rate, 1.0% evaporation rate, and 20% pulse fraction. Data analysis was carried out using the Cameca AP suite 6 and reconstructions were calibrated using crystallographic poles and plane spacings [46]. Precipitate analyses used iso-surface thresholds of 0.7 and 0.9 at% Zr, whereas the solute composition was extracted from core regions with an iso-surface threshold of 5 at% Zr. Particle statistics of radii, number density, and volume fraction were then calculated with the procedure described elsewhere [47].

2.3. Synchrotron x-ray diffraction

High-resolution synchrotron XRD was utilized to identify the phases present in as-fabricated and heat-treated alloys. Data were measured at 11-BM of the Advanced Photon Source at Argonne National Laboratory (Lemont, IL, USA) in a Debye-Scherrer configuration using 0.458105Å x-rays. Diffraction data were measured using powders to ensure the measured data are representative of a bulk average. Powders were obtained by filing test coupons using a diamond file, and resulting powders were loaded into a 1 mm diameter Kapton® tube for the measurement. Diffraction data

were cross-referenced against ternary compounds in Al-Ce-TM (transition metal) systems in the Inorganic Crystal Structure Database (ICSD) [48].

2.4. Mechanical testing

Vickers hardness of the samples was measured at 1 kg load and dwell time of 10 sec. Tensile specimens were machined with a gage diameter of 6.35 mm and axial extensometer gage length of 25.4 mm, in accordance with the ASTM E8 specification. Tensile specimens were not built directly as the resulting properties might be affected by rough surface conditions. The tensile loading axis was parallel to the vertical build direction. Tensile tests were performed between R.T. and 400 °C according to ASTM standards E8 and E21 for R.T. and elevated temperature tests, respectively. A ramp rate of 10 °C/min and a soak time of 30 minutes at temperature to allow for thermal equilibration were used in the tests. An initial strain rate of approximately 10^{-4} s^{-1} was used in all cases, with the strain rate being increased to 10^{-3} s^{-1} after yielding for elevated temperature tests.

2.5. Thermodynamic model and hot-tearing susceptibility

Computer coupling of phase diagrams and thermo-chemistry, i.e., the CALPHAD approach [49] was used to aid understanding of the as-fabricated microstructure. In this approach, the Gibbs energy of individual phases was modeled based on crystal structure, defect type, and phase chemistry. The model parameters were obtained through an optimization procedure that aims to consistently reproduce the experimentally assessed phase equilibria and thermodynamic properties by the model-calculated ones. The Gibbs energy functions of the Al-Cu-Ce system have been modeled by Bo *et al.* [50]. The calculated liquidus projection in Al-rich region in Bo *et al.* 's work showed three primary phases FCC-Al, $Al_{11}Ce_3$, and Al_8Cu_4Ce, which is different from experimental observation [51] i.e., FCC-Al, Al_4Ce, and Al_8Cu_4Ce. It should be noted that Cu has

a large solubility in Al_4Ce. In this work, we use Al_4Ce to represent $(Al,Cu)_4Ce$. On the other hand, the experimental liquidus projection in Al-rich region is not compatible with the liquid surface of $Al_{11}Ce_3$ in the Al-Ce binary. Besides these discrepancies, we also found that a previously unidentified phase is formed in the current AM Al-Cu-Ce and Al-Cu-Ce-Zr alloys. To reconcile the existing discrepancy, we developed new thermodynamic descriptions for phases in Al-rich Al-Cu-Ce system. We also developed a thermodynamic description for the new phase based on the experimental data obtained from this study. The Gibbs energy functions of the three unary systems Al, Ce, and Cu were adopted from the SGTE (Scientific Group Thermodata Europe) database compiled by Dinsdale [52]. The Gibbs energy functions of binary phases were taken from Bo *et al.* [50]. The optimized model parameters for ternary phases are included in the Appendix. The detailed modeling process and the comparison between calculated and experimental data will be presented elsewhere. This work will primarily present results focusing on the calculated solidification path based on the Scheil mode.

The relationship between temperature, T, and the solid fraction, f_s, predicted from the Scheil solidification results were then used to evaluate hot-tearing susceptibility criterion based on an approach proposed by Kou [53]. This criterion considers the average derivative of temperature with respect to the square-root of the solid-fraction. The average is evaluated only within the range of solid-fractions in which the low permeability of a dendritic network limits liquid feeding but before dendrites have coalesced to form a mechanically strong solid structure. This solid-fraction range is not exact, and likely varies depending on alloy and thermal conditions. In the absence of a strict definition of the range, we chose to utilize the same values used by Kou for analyzing Al-Cu based alloys. Kou showed that a range of $0.87 < f_s < 0.94$ produced predictions that were

consistent with hot-tearing susceptibility for welding of Al-Cu alloys. Based on this range, a hot-tearing susceptibility index may be defined as:

$$C_{Kou} = \frac{1}{\Delta f_s} \int_{0.87}^{0.94} \left| \frac{\partial T}{\partial \left(f_s^{1/2} \right)} \right| df_s \quad (1)$$

The thermodynamic model was used to predict the temperature as a function of solid-fraction for a given composition. The square root of the solid-fraction values was then taken, and a spline was fit to the resulting data set within the specified solid-fraction range. The derivative of that spline was then computed and averaged to compute Eq. 1. The thermodynamic model coupled with Scheil solidification model was then used to simulate the solidification behavior for the current Al-Cu-Ce alloy composition and for compositions in the Al-Cu-Ce ternary system with greater than 60 wt% Al in 0.1 wt% increments for both Cu and Ce. The corresponding hot-tearing susceptibility index was computed for each alloy composition as well as several reference alloys (AA2024, AA7075, and AlSi10Mg).

3. Results

3.1. As-fabricated microstructure

Inverse pole figure (IPF) maps of the grain structure in the as-fabricated alloys measured with EBSD are shown in Fig. 1. The Al-Cu-Ce alloy pre-dominantly comprises columnar grains with some regions showing fine equiaxed grains. Addition of Zr resulted in the formation of some coarse equiaxed grains in the microstructure of the Al-Cu-Ce-Zr alloy, as indicated by arrows in Fig. 1c and d. The average grain width is 5 ± 1 and 6 ± 1 μm for Al-Cu-Ce and Al-Cu-Ce-Zr alloys, respectively. The backscatter SEM images of the alloys are shown in Fig. 2. A eutectic structure with FCC-Al and particles of an intermetallic phase is observed. The eutectic structure is largely

similar between the two alloys with subtle differences noted near the melt pool boundary. The inter-particle spacing of the eutectic structure near the melt pool boundary is coarser compared to that away from the boundary in the Al-Cu-Ce alloy, whereas the difference is less between the two regions in the Al-Cu-Ce-Zr alloy. The average inter-particle spacing in the Al-Cu-Ce and Al-Cu-Ce-Zr is 279 ± 43 and 280 ± 48 nm, respectively. The SEM image in Fig. 2e shows primary Al grains in the melt pool interior as indicated by arrows. These grains nucleated heterogeneously on primary Al_3Zr precipitates as shown by an arrow in Fig. 2f and grew into the coarse equiaxed grains observed in the IPF map (Fig. 1c and d) of the Al-Cu-Ce-Zr alloy.

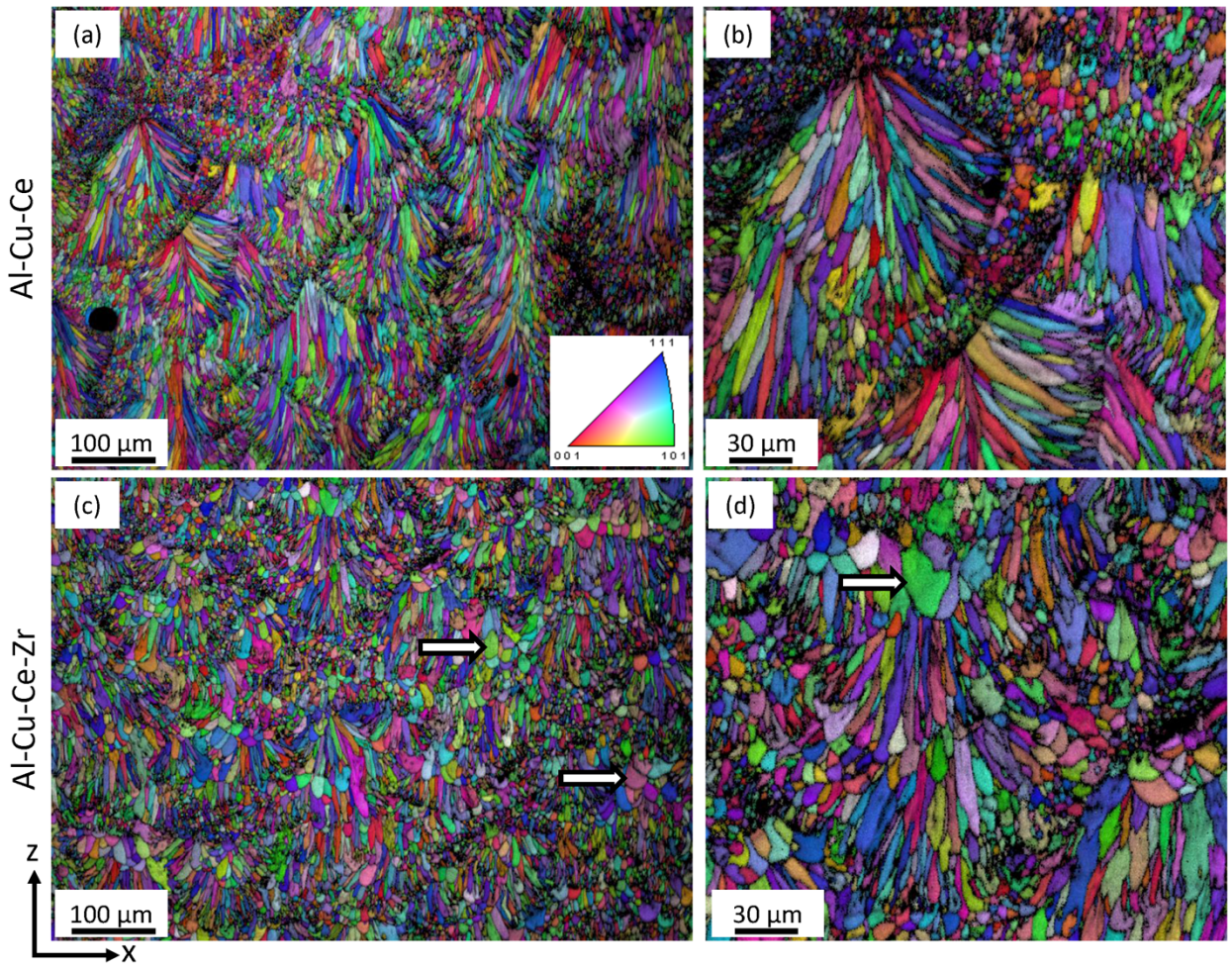

Figure 1 IPF maps showing grain structure in the as-fabricated (a and b) Al-Cu-Ce alloy and (c and d) Al-Cu-Ce-Zr alloy at low and high magnifications. The arrows in (c) and (d) indicate coarse equiaxed grains. The building direction is parallel to the z-axis.

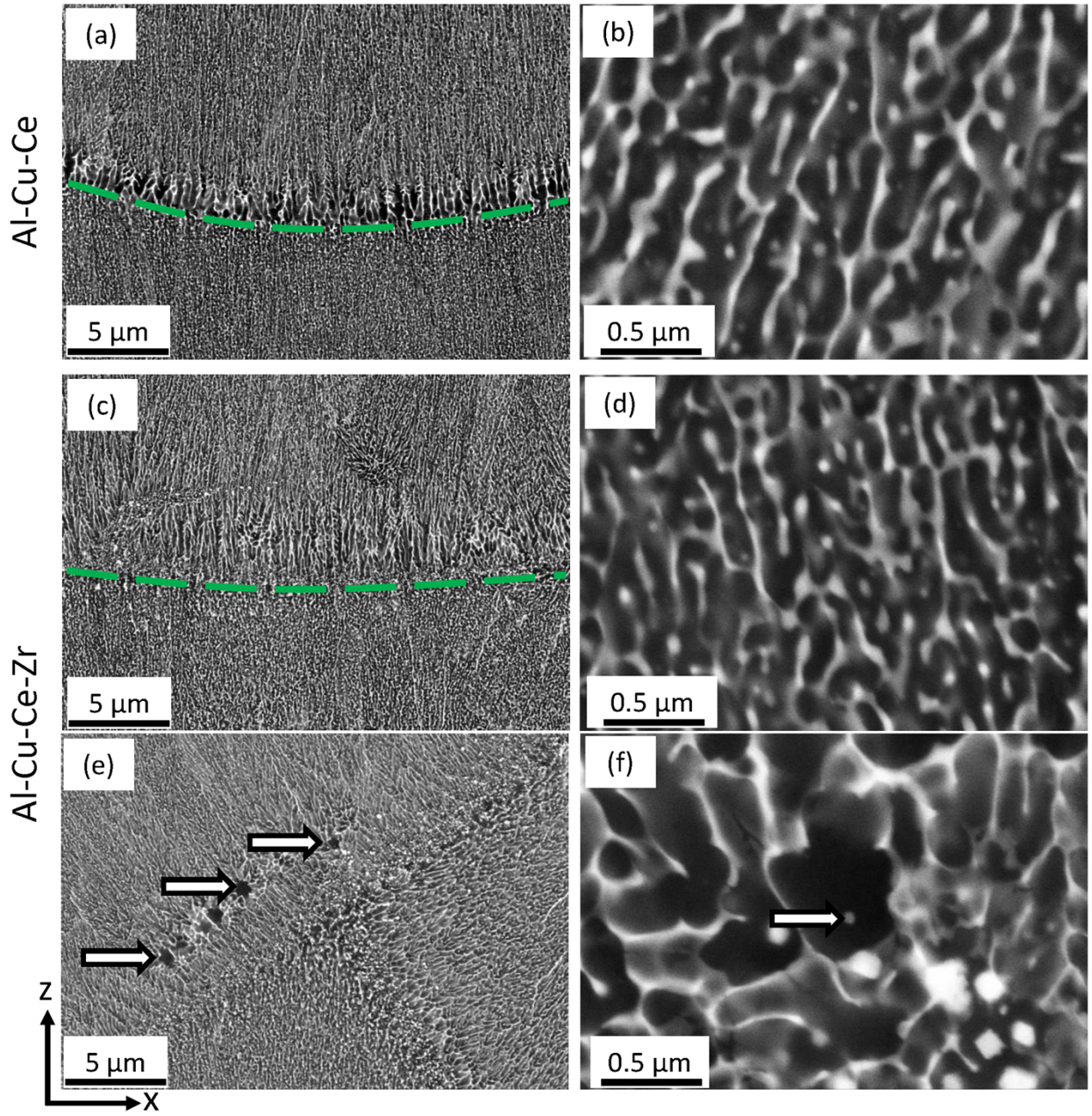

Figure 2 Backscatter SEM images of the eutectic structure in the as-fabricated (a and b) Al-Cu-Ce and (c – f) Al-Cu-Ce-Zr alloys. The dark and bright regions are Al matrix and intermetallic particles, respectively. The curved dashed lines in (a) and (c) mark the melt pool boundaries. The Al grains nucleated on primary $L1_2$ Al_3Zr precipitates in the Al-Cu-Ce-Zr alloy are indicated by arrows in (e) and the arrow in (f) shows one such Al_3Zr precipitate at the center of the equiaxed grain. The building direction is parallel to the z-axis.

The fine scale of the eutectic structure for both alloys is shown in greater detail through the high-angle annular dark-field (HAADF) – STEM images in Fig. 3. The average width of the intermetallic particles determined from the STEM images is 54 ± 14 nm and 55 ± 18 nm for Al-Cu-Ce and Al-Cu-Ce-Zr alloys, respectively. Within the Al portion of this microstructure, high-resolution STEM reveals the presence of a low volume fraction of θ'-Al_2Cu precipitates. The build plate temperature of 200 °C caused an *in situ* aging treatment post-solidification that led to the formation of θ′ precipitates as also reported in our earlier investigation on an AM Al-Cu-Mn-Zr alloy [43]. Similar phase distributions were also observed in the Al-Cu-Ce-Zr alloy. Energy dispersive spectroscopy (EDS) showed that both Cu and Ce elements are enriched in the intermetallic particles.

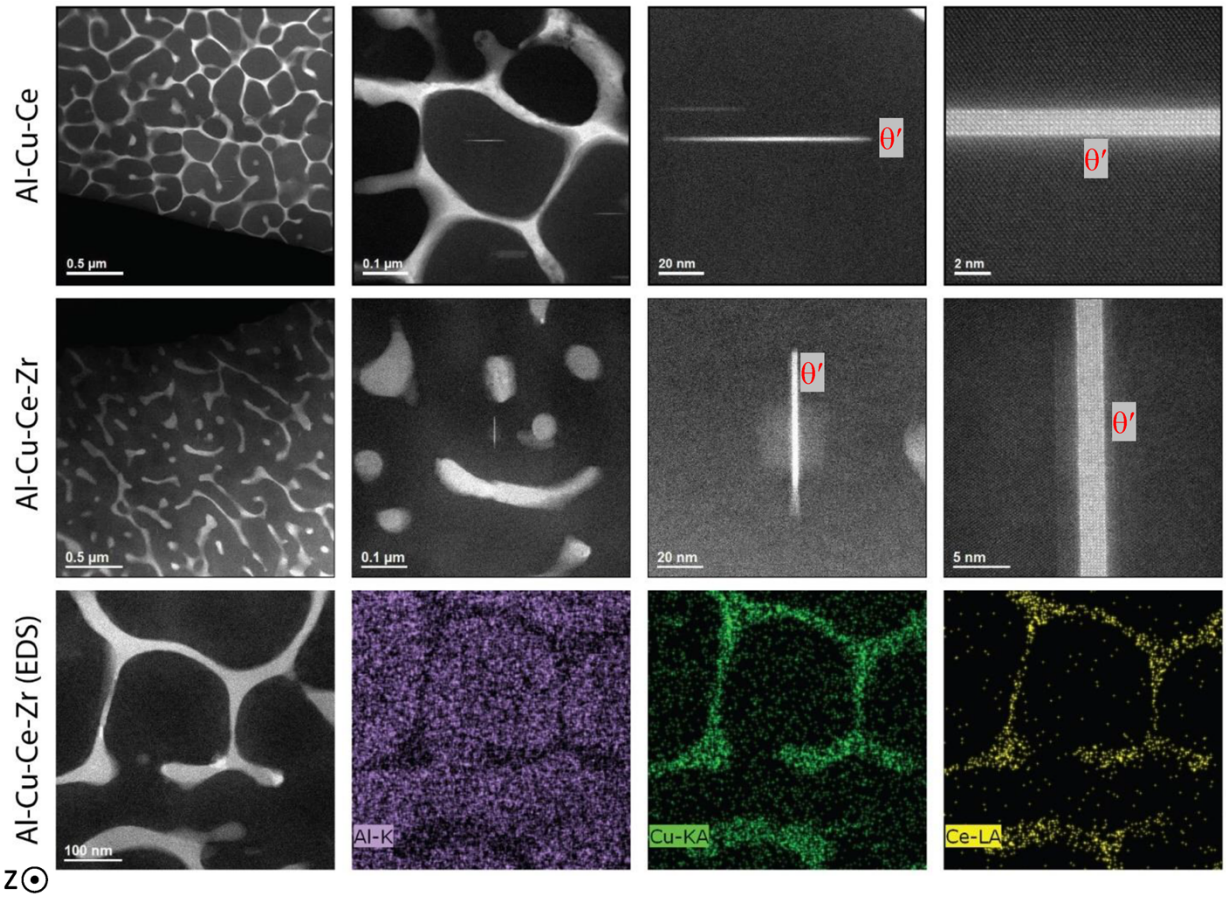

Figure 3 HAADF – STEM images of the as-fabricated Al-Cu-Ce (top row) and Al-Cu-Ce-Zr (middle row) alloys showing the eutectic structure and fine θ' precipitates. The EDS maps of the Al-Cu-Ce-Zr alloy in the bottom row show Cu and Ce enrichment in intermetallic particles. The build direction is normal to the image plane.

The STEM – EDS shown in Fig. 3 is not sufficient to properly quantify the composition of the intermetallic particles, and in particular, the Zr signal was too weak to properly quantify. Therefore, APT was performed on the as-fabricated structure of the Al-Cu-Ce-Zr alloy, with the results summarized in Fig. 4. The APT tip contained cojoined intermetallic particles of different chemistries (IM1 and IM2) embedded within the Al matrix and their composition is shown in Table 3. Both Cu and Ce elements are enriched in these two particles along with small amounts of Zr. In addition, although the two intermetallic particles are composed of the same elements, it is interesting to note that the segregation of impurity element Si is quite different, with Si tending to segregate more strongly to one of the particles.

Table 3 Composition in at% of the intermetallic particles in the as-fabricated Al-Cu-Ce-Zr alloy measured with APT.

Particle	Al	Cu	Ce	Zr	Fe	Si
IM1	69.49 ± 1.75	22.81 ± 1.43	7.6 ± 1.3	0.04 ± 0.16	0.01 ± 0.04	0.08 ± 0.14
IM2	49.71 ± 1.70	24.80 ± 1.60	13.01 ± 1.54	0.19 ± 0.40	0.01 ± 0.04	12.29 ± 1.01

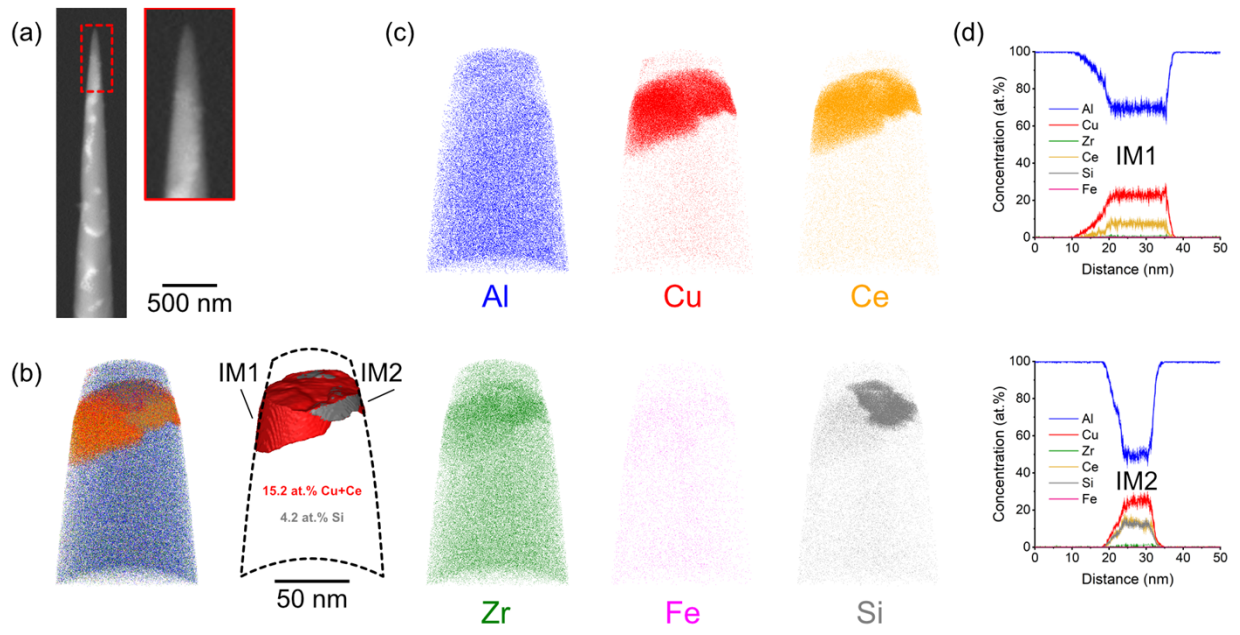

Figure 4 APT results of the as-fabricated microstructure of the Al-Cu-Ce-Zr alloy, showing (a) SEM images of the sectioned APT tip, (b) a hypermap reconstruction of the APT tip along with iso-concentration surfaces used to identify two separate intermetallic particles (IM1 and IM2), (c) elemental distributions for the primary alloying additions as well as for impurity content of Fe and Si, (d) the measured proximity histogram across the intermetallic particles.

3.2. Intermetallic phase identification

Synchrotron x-ray patterns of the as-fabricated Al-Cu-Ce and Al-Cu-Ce-Zr alloys are shown in Fig. 5. The patterns of the two alloys are similar which suggests that the dominant phases present in both are the same. The FCC-Al (111) peak dominates the pattern with the remaining peaks belonging to the intermetallic particles in the eutectic structure. The intermetallic peaks best match those of the quaternary compound $Al_{24}Cu_8Ce_3Mn$ (Pm-3m, a = ~8.51 Å) [54]. However, the present alloys do not contain Mn. Assuming that Cu and Mn substitute, simplifies the quaternary compound to Al_8Cu_3Ce. This simplified composition agrees well with the composition of the intermetallic particle IM1 determined with APT (Table 3). The Si-rich intermetallic particle IM2 (Table 3) either has the same crystal structure as the Al_8Cu_3Ce phase or is present in a minor fraction in the microstructure of the two alloys. Further analysis combining high-resolution STEM

and Rietveld refinement is required to identify the lattice sites for each specific element and obtain an unambiguous structure model.

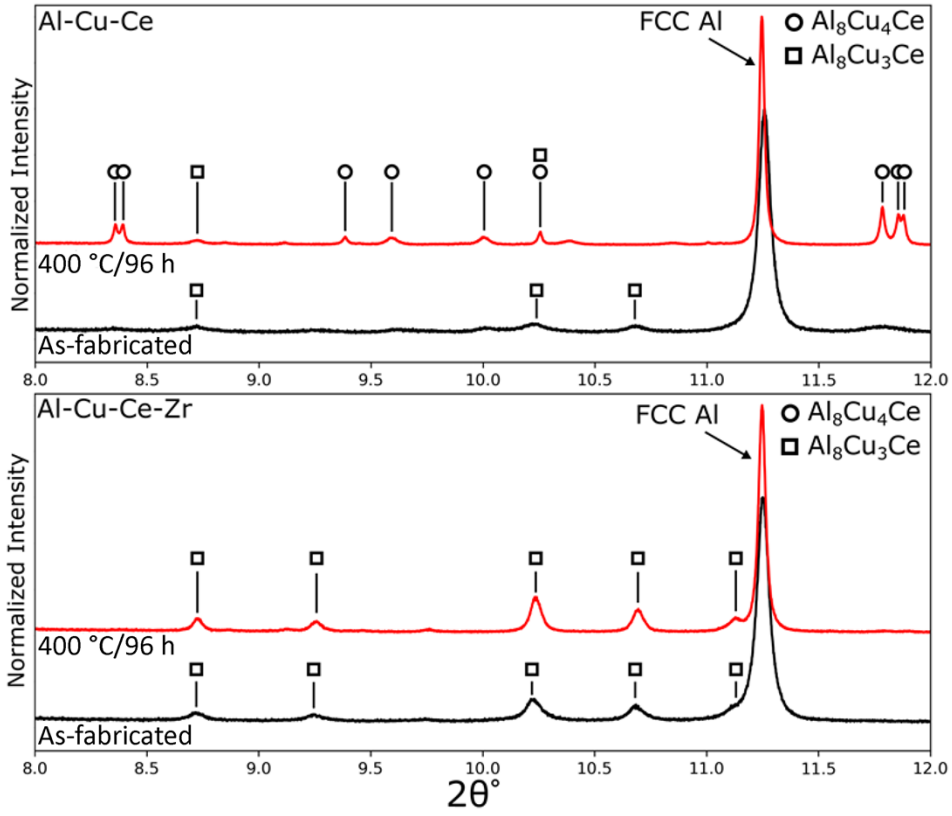

Figure 5 Synchrotron x-ray diffraction patterns of the as-fabricated and 400 °C/96 h heat-treated Al-Cu-Ce and Al-Cu-Ce-Zr alloys. The crystal structure of the intermetallic particles in the as-fabricated condition matches with that of $Al_{24}Cu_8Ce_3Mn$ and are considered compositionally to be Al_8Cu_3Ce. The intermetallic particles transform to Al_8Cu_4Ce in the Al-Cu-Ce alloy but are stable in the Al-Cu-Ce-Zr alloy at 400 °C.

3.3. Heat-treated microstructures

To understand the effects of heat-treatment and extended service life at elevated temperatures, the as-fabricated alloys were exposed to temperatures ranging between 250 – 400 °C for up to 200 h. The SEM images for four temperatures (250, 300, 350, and 400 °C) after 200 h thermal exposures are shown in Fig. 6. In the Al-Cu-Ce alloy, exposure at 250 °C did not produce a noticeable change in the eutectic structure but exposure at higher temperatures caused the intermetallic particles to spheroidize and coarsen. The degree of coarsening can be qualitatively seen to increase with

temperature. The coarsening is also accompanied by phase transformation of the intermetallic particles from the as-fabricated Al_8Cu_3Ce to Al_8Cu_4Ce phase, as shown in the XRD pattern of the 400 °C/96 h heat-treated Al-Cu-Ce alloy (Fig. 5). We note that, while the chemistry is similar, the as-fabricated Al_8Cu_3Ce phase is distinctly different from the more Cu-rich Al_8Cu_4Ce phase formed after heat-treatment. The hardness of the Al-Cu-Ce alloy as a function of exposure time and temperature are shown in Fig. 7a. The horizontal line in Fig. 7a indicates the as-fabricated hardness of the alloy equal to 122 HV1. At 250 °C, an initial drop in hardness to about 115 HV1 after 1 h is followed by only a small decrease over subsequent times, with a minimum of 110 HV1 after 200 h. At 300 °C, a similar initial drop in hardness is observed, but is followed in this case by a steady decrease as a function of time to a minimum of approximately 100 HV1 at 200 h. At higher temperatures of 350 and 400 °C, the initial decrease in hardness is more extreme (90 – 100 HV1), but extended exposure time did not have a dramatic effect. The final hardness at the end of 200 h exposure is roughly similar (90 – 100 HV1) between 300 and 400 °C.

The microstructure and hardness evolution in the Al-Cu-Ce-Zr alloy exhibited a different response. Addition of Zr increased the thermal stability of the Al_8Cu_3Ce intermetallic particles against spheroidization and coarsening as well as phase transformation to the Al_8Cu_4Ce phase. The SEM images in Fig. 6 show that the intermetallic particles are resistant to spheroidization and coarsening up to 350 °C compared to 250 °C for the Al-Cu-Ce alloy. The XRD pattern of the Al-Cu-Ce-Zr alloy after heat-treatment at 400 °C/96 h in Fig. 5 shows that the Al_8Cu_3Ce phase is stable, unlike in the Al-Cu-Ce alloy where phase transformation to Al_8Cu_4Ce occurs. The hardness of the Al-Cu-Ce-Zr alloy as a function of exposure time and temperature are shown in Fig. 7b. The as-fabricated hardness of the Al-Cu-Ce-Zr alloy was slightly higher than the Al-Cu-Ce alloy, increasing to 128 HV1. At 250 °C, there was a small initial drop in hardness, but no substantial

change with additional exposure time. For thermal exposure at 300 °C, the hardness remained similar to the as-fabricated condition for 24 h, and then began to rise, reaching a maximum value of 150 HV1 after 200 h. For a higher temperature of 350 °C, the peak hardness occurred at 8 h and decreased marginally at extended exposure times. At 400 °C, the peak condition was observed after only 1 h and the hardness decreased rapidly with extended exposure.

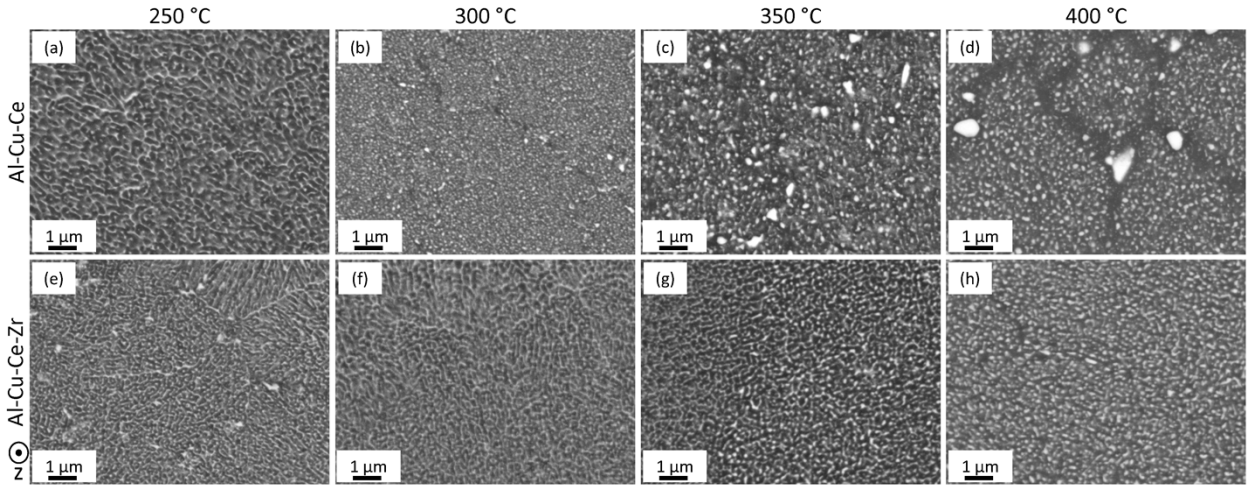

Figure 6 SEM images of the (a – d) Al-Cu-Ce and (e – h) Al-Cu-Ce-Zr alloys after 200 h heat-treatment at temperatures between 250 – 400 °C. The improved thermal stability of the intermetallic particles in the Al-Cu-Ce-Zr alloy relative to the Al-Cu-Ce alloy can be seen in these images. The build direction is normal to the image plane.

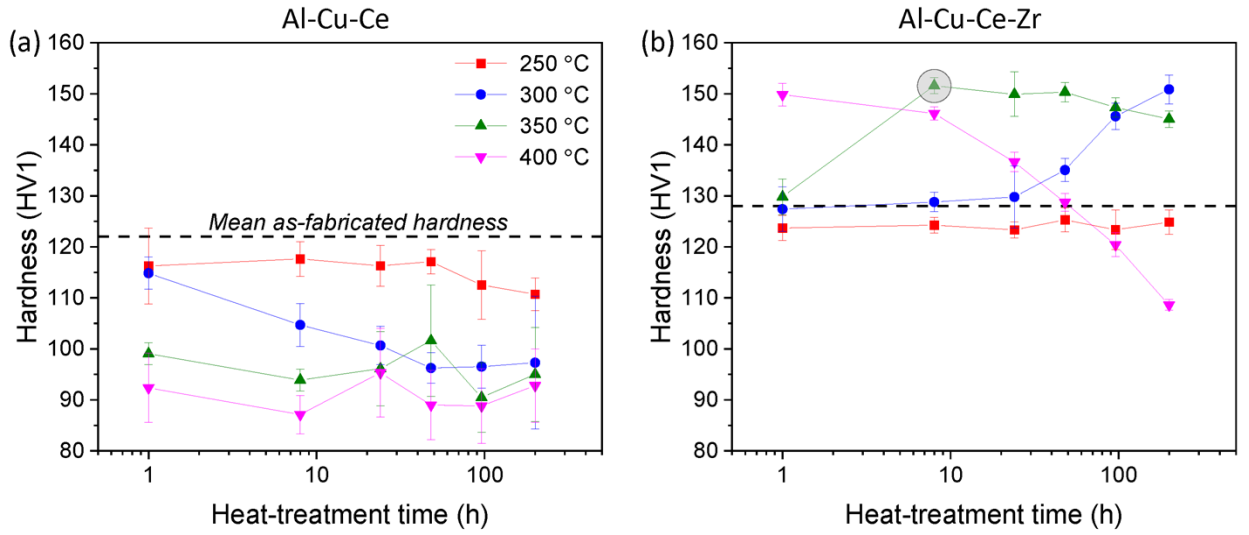

Figure 7 Evolution of Vickers hardness in the (a) Al-Cu-Ce and (b) Al-Cu-Ce-Zr alloys as a function of heat-treatment time and temperature. The temperature legend in (a) also applies to (b).

The addition of Zr produced an age-hardening response in the Al-Cu-Ce-Zr alloy. The grey circle in (b) highlights the peak-aged condition that was chosen for APT characterization and tensile testing.

3.4. APT on peak-aged Al-Cu-Ce-Zr alloy

Based on the hardness results, the peak-aged condition of 350 °C/8 h was selected for APT analysis to assess the microstructural features responsible for the hardening response of the Al-Cu-Ce-Zr alloy. APT needles were extracted from regions near the melt pool boundary and away from the melt pool boundary, reconstructions of which are shown in Fig. 8a and c, respectively. Zr iso-concentration surfaces show nanoscale Zr-rich precipitates embedded within the Al matrix of the peak-aged microstructure. The mean particle compositions near the melt pool boundary and away from it are Al-31Zr (at%) and Al-28Zr (at%), respectively, consistent with the expected composition of Al_3Zr $L1_2$ nano-precipitates. The size, number density, and volume fraction of the precipitates are summarized in Table 4. The volume fraction and number density of Al_3Zr precipitates are slightly higher and the size smaller near the melt pool boundary compared to the region away from the boundary. The solute concentrations in the Al matrix of the peak-aged condition are compared to that in the as-fabricated condition for similar locations with respect to the melt pool boundary in Fig. 8b and d. In the as-fabricated Al matrix, the Zr concentration is marginally higher near the melt pool boundary than that away from it, which is consistent with the higher volume fraction of Al_3Zr precipitates near the boundary in the peak-aged condition (Table 4). Solutes including Cu and Si are present in trace amounts in the as-fabricated Al matrix. Note that there is no conclusive evidence of any notable solubility of Ce in Al. The concentration of all the solutes reduces to near-zero levels in the peak-aged condition indicating a virtually solute-free Al matrix.

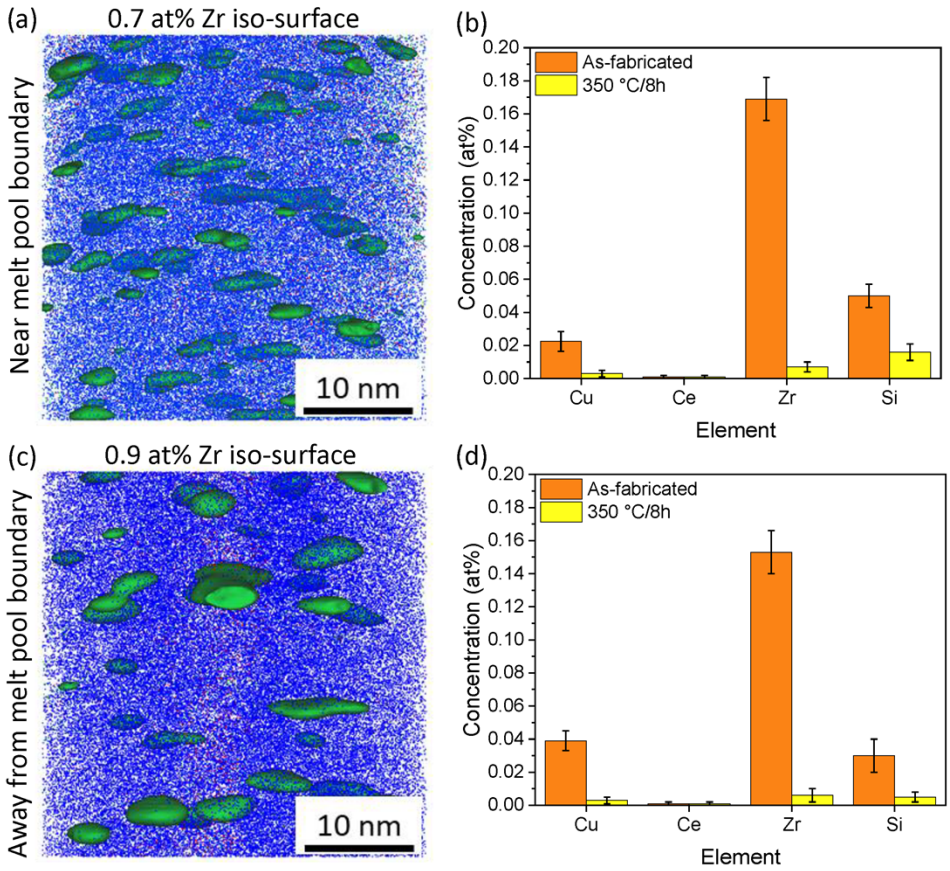

Figure 8 APT atom map of the peak-aged (350 °C/8h) Al-Cu-Ce-Zr alloy showing Al_3Zr precipitates in regions (a) near melt pool boundary and (c) away from melt pool boundary. Al atoms are shown in blue and Zr atoms in green. The Al matrix composition in the peak-aged and as-fabrciated conditions for regions (b) near melt pool boundary and (d) away from melt pool boundary.

Table 4 APT quantification of Al_3Zr precipitates in the peak-aged (350 °C/8h) Al-Cu-Ce-Zr alloy. The mean and standard deviation values are reported.

Parameter	Near melt pool boundary	Away from melt pool boundary
Volume fraction, f (%)	0.67 ± 0.05	0.60 ± 0.17
Radius, r (nm)	0.93 ± 0.03	1.05 ± 0.05
Number density, N ($\times 10^{24}$ m^{-3})	2.0 ± 0.3	1.3 ± 0.5

3.5. Tensile properties

The yield and ultimate tensile strength of the Al-Cu-Ce and Al-Cu-Ce-Zr alloys are compared as a function of temperature in Fig. 9a, b. It is noted that tensile properties of the as-fabricated Al-Cu-Ce alloy along with ductility results of the as-fabricated Al-Cu-Ce-Zr alloy were reported in our recent investigation on the phenomenon of elevated temperature ductility dip in these alloys [44]. In the as-fabricated condition, the yield strength of the two alloys is similar up to 300 °C but is higher for the Zr modified alloy at 400 °C (Fig. 9a). The properties of the peak-aged (350 °C/8h) Al-Cu-Ce-Zr alloy were measured at R.T. and 300 °C. The peak-aged alloy exhibits a significant improvement in the yield strength at R.T. but only a marginal improvement at 300 °C relative to the as-fabricated condition. The performance of the current alloys is benchmarked against AlSi10Mg and Al-Mg-Sc (Scalmalloy) alloys fabricated with LPBF additive manufacturing. The properties of AlSi10Mg were taken from elsewhere [38]. These samples were soaked at test temperature for 10 min prior to testing and tested at a strain-rate of approximately 4.8×10^{-4} s^{-1}. The properties for Scalmalloy were taken from the alloy data sheet in which the test conditions were not specified [55]. The yield strength of the as-fabricated Al-Cu-Ce and Al-Cu-Ce-Zr alloys is higher than AlSi10Mg in the entire R.T. – 400 °C temperature range with the difference more pronounced at and above 300 °C. The as-fabricated alloys show higher yield strength compared to Scalmalloy at temperatures greater than 200 °C, while the trend is opposite at lower temperatures. The peak-aged Al-Cu-Ce-Zr alloy has higher yield strength compared to both AlSi10Mg and Scalmalloy at 300 °C, but the yield strength at R.T.is higher compared only to AlSi10Mg.

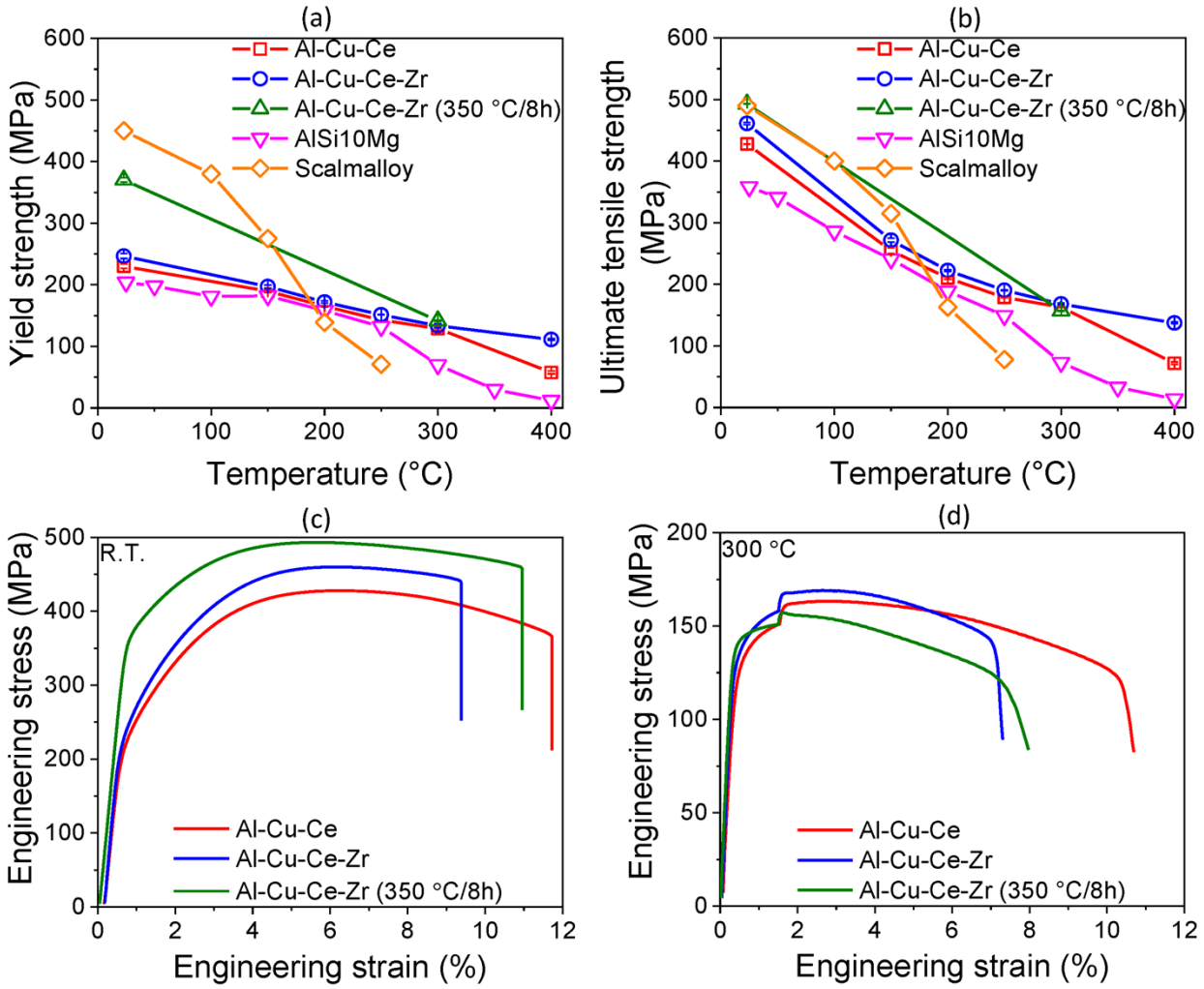

Figure 9 (a) Yield strength and (b) ultimate tensile strength of the as-fabricated Al-Cu-Ce and Al-Cu-Ce-Zr and peak-aged (350 ℃/8h) Al-Cu-Ce-Zr alloys. Properties of AlSi10Mg and Scalmalloy are also shown [38, 55]. Engineering stress-strain curves of the alloys at (c) R.T. and (d) 300 ℃.

4. Discussion

4.1. As-fabricated microstructure formation

A thermodynamic model including the newly identified Al_8Cu_3Ce intermetallic phase was developed to compute Scheil solidification curve for the Al-Cu-Ce alloy as shown in Fig. 10a. Note that the experimentally measured alloy composition Al-7.78Cu-4.73Ce (wt%) was used in the thermodynamic model. According to the Scheil model, solidification begins with primary FCC-Al phase, followed briefly by Al and Al_4Ce eutectic, which then transitions to Al and

Al_8Cu_3Ce eutectic. The solidification ends with a small fraction of ternary eutectic comprising Al, Al_8Cu_3Ce, and Al_2Cu phases. The calculated mole fractions of phases from the Scheil model are ~0.88 (Al), 0.09 (Al_8Cu_3Ce), 0.01 (Al_4Ce) and 0.02 (Al_2Cu), respectively, which is consistent with the experimentally observed major phases Al and Al_8Cu_3Ce (Fig. 5) in the as-fabricated condition. The phases Al_4Ce and Al_2Cu predicted by the Scheil model could not be experimentally verified possibly due to their low phase fractions. The thermodynamic database suggests that the alloy composition is hypoeutectic (Fig. 10a) relative to the binary L → Al + Al_8Cu_3Ce reaction. However, the microstructure is mostly eutectic in morphology, suggesting that the non-equilibrium conditions in AM tends to favor suppression of Al dendrites in favor of eutectic solidification. This observation is likely the result of an enlarged eutectic coupled zone for high solidification rates as a result of significant undercooling at the solid-liquid interface [56, 57]. Similar observations have been made for an Al-Ce-Mn alloy as a function of distance from the melt pool boundary [30], and is qualitatively similar to the microstructure selection theory used to explain non-equilibrium solidification microstructures in welding [29, 58-60]. Further study is needed to properly quantify the selection of such non-equilibrium microstructure for the complex thermal conditions in additive manufacturing processes, and for the present alloys.

The Scheil curve of the Al-Cu-Ce alloy is compared with those of AM AlSi10Mg and wrought AA2024 and AA7075 Al alloys in Fig. 10b and the hot-tearing susceptibility index calculated from these curves according to Eq. 1 is shown in Fig. 10c. The wrought alloy compositions exhibit the highest hot-tearing susceptibility among the alloys considered. AlSi10Mg, which is a highly processable alloy, shows a significant reduction in hot-tearing susceptibility compared to the wrought alloys, consistent with its early adoption within the AM industry. The present Al-Cu-Ce alloy composition exhibits an even lower hot-tearing susceptibility, suggesting superior

processability of the alloy. Scheil simulations were also performed at 0.1 wt% intervals over the Al-rich region (> 60 wt% Al) corner of the Al-Cu-Ce system, and the hot-tearing susceptibility was computed for each composition. The resulting distribution of hot-tearing susceptibility is shown in Fig. 10d. Overall, this portion of the phase diagram is generally resistant to hot-tear cracking except for a narrow region in the middle. The Al-Cu-Ce system appears to be highly promising in that the wide range of alloy compositions with potentially superior processability offers the possibility to tune the microstructure and mechanical properties in Al-Cu-Ce alloy system.

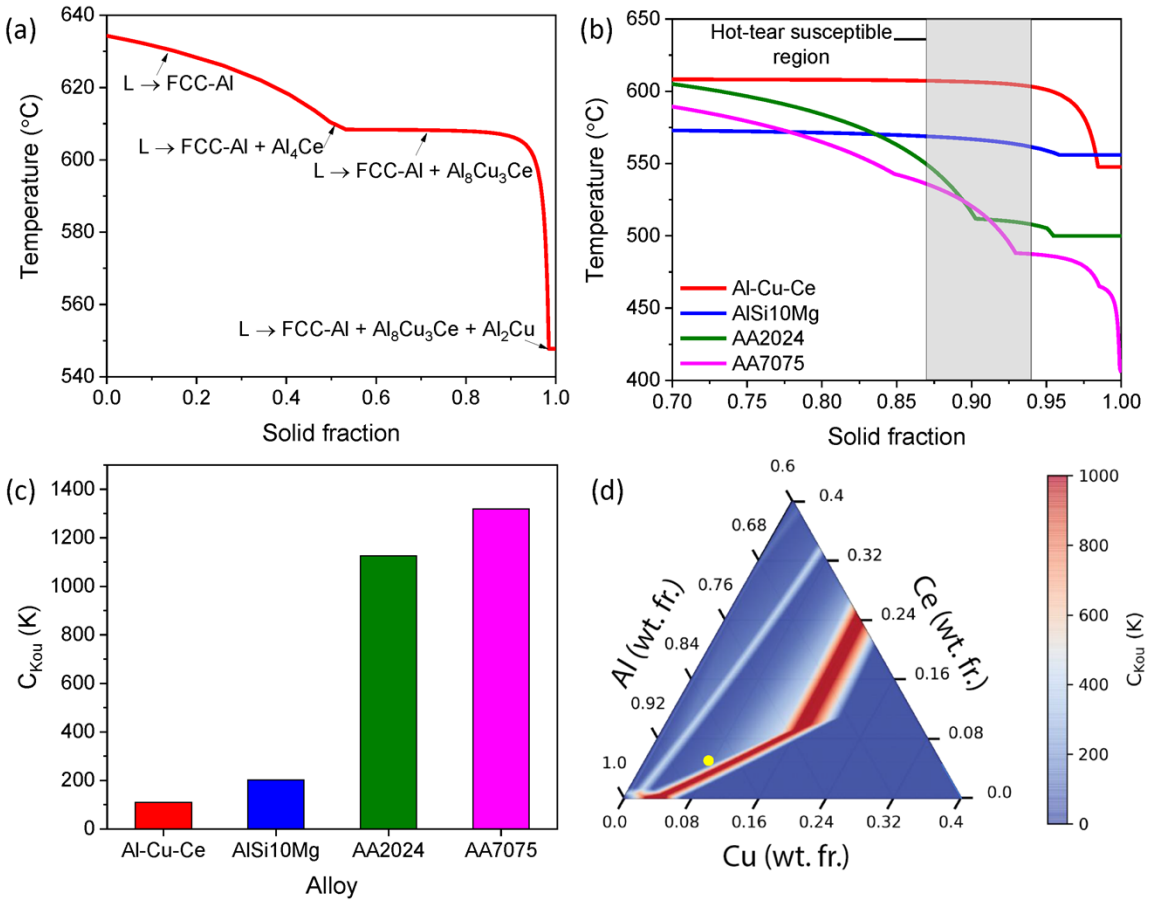

Figure 10 (a) Scheil curve for the Al-7.78Cu-4.73Ce alloy, (b) segment of the same Scheil curve at high solid fractions compared to those of AlSi10Mg, AA2024, and AA7075 Al alloys. The shaded region marks the range of solid fraction over which the hot-tearing susceptibility index was calculated. (c) The hot-tearing susceptibility index for the four alloys, and (d) the distribution of

hot-tearing susceptibility index calculated for Al-rich corner of the Al-Cu-Ce phase diagram. The dot indicates the Al-7.78Cu-4.73Ce alloy composition.

Zr modification in the Al-Cu-Ce alloy did not alter the eutectic structure or the intermetallic phase in the as-fabricated condition. Interestingly, widespread formation of primary Al_3Zr precipitates and the resultant nucleation of equiaxed Al grains was not observed in the Al-Cu-Ce-Zr alloy. This behavior is in contrast to AM Al-Mg, Al-Mn, and Al-Zn based alloys modified with Zr and/or Sc in which copious amounts of primary Al_3(Zr, Sc) precipitates formed at low solid-liquid interface velocities near the melt pool boundaries nucleate bands of equiaxed Al grains in that region [13, 15, 39, 40, 61, 62]. One possible reason for the suppressed precipitation of primary Al_3Zr could be due to a larger undercooling required for their nucleation compared to the undercooling required for growth of the eutectic front in the present alloy. However, additional research will be necessary to properly quantify this competition. Since primary Al_3Zr precipitates were largely suppressed, Zr remained supersaturated in the Al matrix. Zr concentration of 0.169 at% in the as-fabricated Al matrix in nearly two times higher than the solid-solubility limit of 0.083 at% in a binary Al-Zr alloy [41]. The effect of this high Zr supersaturation on the precipitation of secondary Al_3Zr nanoscale precipitates is discussed in the next section.

4.2. Heat-treated microstructure

The microstructural stability and hardness of the two alloys were examined as a function of heat-treatment time and temperature. The intermetallic particles in the as-fabricated Al-Cu-Ce alloy were stable at 250 °C evident from the SEM image (Fig. 6a) and relatively small drop in hardness after 200 h of exposure (Fig. 7a). At temperatures between 300 – 400 °C (Fig. 6b-d), the intermetallic particles in the eutectic structure spheroidized and coarsened and that contributed to the drop in hardness (Fig. 7a). Although the hardness dropped faster with time as the temperature increased, the final hardness after 200 h exposure was similar between 300 – 400 °C and

approximately equal to 75% of the as-fabricated hardness. Such a high hardness retention demonstrates remarkable coarsening resistance of the intermetallic particles in the Al-Cu-Ce alloy up to 400 °C, primarily owed to the negligible solid-solubility of Ce in the Al matrix. Cu is not expected to contribute to thermal stability because of its higher solid-solubility and diffusivity in Al matrix compared to Ce [26]

Addition of Zr improved the coarsening resistance of the intermetallic particles from 250 °C in the Al-Cu-Ce alloy to 350 °C in the Al-Cu-Ce-Zr alloy (Fig. 6). At 400 °C, the intermetallic particles coarsened but the extent was visibly less relative to the Al-Cu-Ce alloy. The phase transformation from Al_8Cu_3Ce to Al_8Cu_4Ce was also inhibited through Zr addition (Fig. 5). The coarsening of a secondary phase can be rate-limited by the slowest diffusing component in that phase [63]. It is possible that presence of the slow diffusing Zr in the intermetallic phase (Fig. 4, Table 3) enhanced its thermal stability, however, the exact mechanism needs further investigation. It also appears that the inhibited phase transformation of the particles is related to the improved coarsening resistance. Heat-treatment between 300 – 400 °C produced a significant age-hardening response due to precipitation of secondary Al_3Zr precipitates (Fig. 7b). The hardness did not increase at 250 °C suggesting lack of appreciable Al_3Zr precipitation. The peak-aged hardness values were similar between 300 – 400 °C but accelerated kinetics reduced the exposure time to obtain the peak hardness with increase in temperature. At 400 °C, the hardness reduced continuously from its peak-aged value at higher exposure times suggesting coarsening of both Al_3Zr precipitates and intermetallic particles in the eutectic. At 350 °C, the peak-aged hardness was relatively stable with time suggesting high coarsening resistance of Al_3Zr precipitates and intermetallic particles. The hardness at 300 °C continued to exhibit an upward trend at the end of 200 h exposure and may increase further at higher exposure times. The Al_3Zr precipitates in the peak-aged condition (350

°C/8h) have a ~ 2 – 3 times higher volume fraction, ~10 times higher number density, and ~ 2 – 3 times smaller radius compared to $L1_2$ precipitates in the peak-aged cast Al alloys [64-66]. This higher volume fraction of Al_3Zr precipitates is a consequence of the enhanced Zr supersaturation in the Al matrix caused by rapid solidification of the alloy. Zr supersaturation was slightly higher in the Al matrix near the melt pool boundary (Fig. 8) which likely increased the nucleation rate of Al_3Zr precipitates and resulted in their finer size relative to precipitates away from the boundary [67].

4.3. Microstructure-property correlations

Theoretical models were used to analyze strengthening mechanisms in the as-fabricated (Al-Cu-Ce/Al-Cu-Ce-Zr) and peak-aged (Al-Cu-Ce-Zr) alloys. The eutectic structure was considered to strengthen by the Orowan mechanism in which dislocations bypass the intermetallic particles by looping around them. The Orowan strengthening $\Delta\sigma_{oro}$was approximated using the following equation valid for spherical particles [68]:

$$\Delta\sigma_{oro} = \frac{MG_{Al}b}{2\pi\lambda\sqrt{1-\nu}} \ln\left(\frac{d_p}{b}\right) \quad (2)$$

where, M is the Taylor factor for FCC structure (3.06), G_{Al} is the shear modulus of Al matrix (25 GPa), b is the Burgers vector of Al matrix (0.286 nm), ν is Poisson's ration (0.345), λ is the inter-particle spacing, and d_p is the planar diameter of the particle in the slip plane. The thickness of the intermetallic particles was approximated as the planar diameter of the particle. The grain size strengthening was measured by the Hall-Petch equation given by [69]:

$$\Delta\sigma_{HP} = kd^{-1/2} \quad (3)$$

where, k is a constant (0.04 MPa √m for Al) and d is the grain size. An upper bound of grain size strengthening was calculated by approximating the grain size with the width of columnar grains

measured from the IPF maps (Fig. 1). Solid-solution strengthening was ignored due to low solute concentrations in the Al matrix.

The mean inter-particle spacing, particle thickness, and grain width for Al-Cu-Ce and Al-Cu-Ce-Zr alloys are mentioned in Section 3.1. The calculated values of Orowan and grain size strengthening are 80 MPa and 16 MPa, respectively. Although Orowan strengthening does not explain the complete yield strength (230 – 250 MPa), it is a major strengthening mechanism in these alloys. This result can be contrasted with cast Al-12.5Ce (wt%) alloy with the total alloy content similar to the present alloys, in which strengthening from the coarse eutectic structure with micron sized spacing was less than 20 MPa [27]. Thus, AM can produce bulk high-strength eutectic alloys through microstructural refinement at high solidification rates that is challenging to achieve with conventional materials processing routes. The fine eutectic structure in the present alloys is relatively stable at elevated temperatures owing to the high coarsening resistance of the intermetallic particles. As a result, the alloys retain a high fraction of their R.T. yield strength at elevated temperatures and outperform baseline AlSi10Mg and Scalmalloy. The total yield strength is not calculated and compared to the experimental value as there appears to be additional sources of strengthening in the as-fabricated alloys. These mechanisms may include composite strengthening from the high volume fraction of load bearing intermetallic particles, dislocation strengthening, and precipitation strengthening from θ′ precipitates. Accurate determination of these strengthening mechanisms is beyond the scope of the present investigation. The composite strengthening can be possibly quantified using in situ x-ray/neutron tensile testing combined with either analytical or finite element modeling [70, 71]. X-ray line profile analysis can statistically determine dislocation density needed for strengthening calculations [72]. The estimation of θ′

strengthening will need careful TEM measurements of precipitate dimensions and volume fraction [73].

Al_3Zr precipitates in the peak-aged Al-Cu-Ce-Zr alloy can strengthen either by dislocation shearing or dislocation bypass (Orowan strengthening) mechanisms such that the weaker of the two mechanisms prevails. The Orowan strengthening from Al_3Zr precipitates was calculated using Eq. 2. The planar diameter d_p is equal to $\frac{\pi d}{4}$ where, d is the Al_3Zr diameter determined from APT (Table 4). The inter-particle spacing was calculated assuming a triangular array of precipitates in the slip plane and is given by the following equation:

$$\lambda = \left(\frac{0.779}{\sqrt{f}} - 0.785\right)d \tag{4}$$

where f is the volume fraction of Al_3Zr precipitates. Strengthening from dislocation shearing can occur due to coherency strain of the precipitates ($\Delta\sigma_{coh}$), modulus mismatch between matrix and precipitate ($\Delta\sigma_{mod}$), or order strengthening upon formation of anti-phase boundary (APB) ($\Delta\sigma_{ord}$) [74-76]. The order strengthening occurs serially to coherency and modulus strengthening, as a result of which, the net strengthening from dislocation shearing is determined by the maximum between order strengthening and sum of coherency and modulus strengthening. Strengthening from these mechanisms is calculated by the following equations:

$$\Delta\sigma_{coh} = M\chi(\epsilon G_{Al})^{3/2}\left(\frac{rfb}{\Gamma}\right)^{1/2} \tag{5}$$

$$\Delta\sigma_{mod} = 0.0055Mb(\Delta G)^{3/2}\left(\frac{f}{\Gamma}\right)^{1/2}\left(\frac{r}{b}\right)^{\frac{3m}{2}-1} \tag{6}$$

$$\Delta\sigma_{ord} = 0.81M\left(\frac{\gamma_{APB}}{2b}\right)\left(\frac{3\pi f}{8}\right)^{1/2} \tag{7}$$

where, r is the precipitate radius, χ is equal to 2.6, ϵ is constrained lattice parameter mismatch between Al_3Zr and Al matrix given by $\frac{2}{3}.\frac{\Delta a}{a}$ with $\frac{\Delta a}{a}$ equal to 0.0075 for Al_3Zr, Γ is dislocation line tension in Al given as $\frac{1}{2}G_{Al}b^2$, ΔG is the shear modulus difference between Al (25 GPa) and Al_3Zr (68 GPa) [77], m is a constant equal to 0.85, γ_{APB} is the APB energy equal to 0.445 J/m^2 for Al_3Zr precipitate [78]. The characteristics of Al_3Zr precipitates for the region away from the melt pool boundary were used in these calculations (Table 4). The results of the strengthening calculations are summarized in Table 5 which suggest that Al_3Zr precipitates strengthen primarily by a dislocation shearing mechanism in the Al-Cu-Ce-Zr alloy. The similar magnitudes of order strengthening and the sum of coherency and modulus strengthening makes exact determination of the strengthening mechanism difficult. The 157 – 163 MPa of calculated precipitation strengthening is more than the 123 MPa increase measured in the R.T. yield strength of the peak-aged Al-Cu-Ce-Zr alloy compared to its as-fabricated condition. The strengthening from Al_3Zr precipitates is counterbalanced by possible loss in strengthening from recovery of dislocations and dissolution of θ′ precipitates during aging at 350 °C. It is interesting to note that yield strength of the peak-aged Al-Cu-Ce-Zr alloy did not improve at 300 °C despite the presence of nanoscale Al_3Zr precipitates. A similar result was reported by Griffiths *et al.* [12] in which a peak-aged Al-Mg-Zr alloy comprising nanoscale Al_3Zr precipitates displayed lower strength than the as-fabricated alloy at elevated temperatures. The poor strength in that case was attributed to enhanced grain boundary sliding caused by coarsening of grain boundary intermetallic particles during the aging treatment. It is not clear whether a similar phenomenon is active in the Al-Cu-Ce-Zr alloy. Although intermetallic particles in the bulk are stable at 350 °C in the Al-Cu-Ce-Zr alloy, accelerated coarsening of the intermetallic particles at the grain boundaries is possible, which is not captured accurately in the SEM images. Further investigation is needed to understand the

deformation mechanisms and lack of strengthening thereof in the peak-aged alloy at elevated temperatures.

Table 5 Calculated values of different strengthening mechanisms possible with Al_3Zr precipitates in the peak-aged (350 °C/8h) Al-Cu-Ce-Zr alloy.

Strengthening mechanism	Value (MPa)
Coherency ($\Delta\sigma_{coh}$) + Modulus mismatch strengthening ($\Delta\sigma_{mod}$)	157
Order strengthening ($\Delta\sigma_{ord}$)	163
Orowan strengthening ($\Delta\sigma_{oro}$)	392

4.4. Implications for future alloy development

The elevated temperature strength of the Al-Cu-Ce(-Zr) alloys depend significantly on the spacing and thermal stability of the intermetallic particles in the eutectic structure. Further refinement in the spacing and increase in thermal stability of the particles can improve the elevated temperature strength of these alloys. The inter-particle spacing in a eutectic is inversely proportional to solid-liquid interface velocity which in turn increases with laser scanning speed during AM [56]. Thus, higher laser scanning speed can potentially lead to alloys with increased strength. The particle spacing can also be refined by tuning alloy composition to increase particle volume fraction or use of additional elements that alter the intrinsic eutectic solidification behavior [79]. A systematic investigation with controlled variation in Cu and Ce contents would be useful in optimizing mechanical properties and also understanding the effect of individual elements on strengthening in Al-Cu-Ce based alloys. Fundamental insights into the mechanism by which Zr increases the thermal stability of the particles will help in design of more thermally stable alloys. For instance, if thermal stability of the particles is related to slow diffusivity of Zr in Al matrix, addition of even

slower diffusers like Ti, V, Cr can further enhance the thermal stability [41]. The lack of strengthening at elevated temperature despite the presence of nanoscale Al_3Zr precipitates is worth noting. Better understanding into elevated temperature deformation mechanisms can guide future alloy design for improving the strength of the current alloys. AM Al alloys may exhibit anisotropic tensile properties [80-82]. The anisotropy in Al-Cu-Ce(-Zr) alloys as a function of temperature and the effect of Al_3Zr precipitates needs to be investigated in future.

5. Conclusions

Microstructure and mechanical properties of Al-9Cu-6Ce and Al-9Cu-6Ce-1Zr (wt%) alloys fabricated with laser powder bed fusion additive manufacturing (AM) were investigated. Important conclusions drawn from this work are the following:

1) The alloys demonstrated excellent processability with > 99.5% relative density. The theoretical hot-tearing resistance of the Al-Cu-Ce alloy was higher than benchmark AM AlSi10Mg alloy suggesting favorable processability.

2) Both alloys solidified with a eutectic structure comprising FCC-Al and particles of a new intermetallic phase identified to be Al_8Cu_3Ce. The rapid solidification in AM produced an ultra-fine eutectic with an inter-particle spacing of approximately 280 nm.

3) The Al-Cu-Ce alloy exhibited remarkable thermal stability with 75% of the as-fabricated hardness retained after 200 h exposure at 400 °C owing to the high coarsening resistance of the intermetallic particles. The high coarsening resistance combined with the ultra-fine eutectic structure improved the elevated temperature (T > 200 °C) strength of the as-fabricated alloys surpassing baseline AlSi10Mg and Scalmalloy.

4) Rapid solidification in AM enhanced Zr supersaturation in Al matrix of the as-fabricated Al-Cu-Ce-Zr alloy. Peak-aging the alloy at 350 °C led to the precipitation of a high number density

(1.3×10^{24} m^{-3}) and volume fraction (0.60%) of small (~ 1 nm radii) Al_3Zr precipitates. The aged microstructure was thermally stable at 350 °C and exhibited a 13% higher hardness after 200 h exposure compared to the as-fabricated alloy. While the peak-aged alloy displayed significant improvement in the room temperature yield strength, the increase in yield strength was small at 300 °C compared to the as-fabricated condition.

This work demonstrates the application of rapid solidification in AM to produce thermally stable bulk eutectic Al alloys with refined microstructures and exceptional mechanical properties that are challenging to achieve via conventional materials processing routes.

Acknowledgements

Research was co-sponsored by the U.S. Department of Energy, Office of Energy Efficiency and Renewable Energy, Advanced Manufacturing Office and Vehicle Technologies Office, Propulsion Materials Program. This research used resources of the Advanced Photon Source; a U.S. Department of Energy (DOE) Office of Science User Facility operated for the DOE Office of Science by Argonne National Laboratory under Contract No. DE-AC02-06CH11357. The authors acknowledge the facilities, as well as the scientific and technical support of the Microscopy Australia nodes at the University of Sydney (Sydney Microscopy & Microanalysis) and at UNSW Sydney (Mark Wainwright Analytical Centre). S. Primig is supported by the Australian Research Council's DECRA (DE180100440) and the UNSW Scientia Fellowship schemes.

Appendix

Model parameters for ternary phases in Al-Cu-Ce system that were optimized in this work. $GHSERAL, GHSERCU, and\ GHSERCE$ were taken from SGTE pure element database.

$$G^0_{Al8Cu4Ce} = 0.6154GHSERAl + 0.3077GHSERCU + 0.0769GHSERCE - 28491$$

$$G^0_{Al8Cu3Ce} = 0.6667GHSERAl + 0.25GHSERCU + 0.0833GHSERCE - 14643 - 13.4T$$

$$G^0_{Al4Ce,Al:Ce} = 0.8GHSERAl + 0.2GHSERCE - 29557 + 2T$$

$$G^0_{Al4Ce,Cu:Ce} = 0.8GHSERCU + 0.2GHSERCE$$

$$G^0_{Al4Ce,Al,Cu:Ce;0} = -80060 + 20T$$

$$G^0_{Al4Ce,Al,Cu:Ce;1} = -65060 + 20T$$

References

[1] W.J. Sames, F.A. List, S. Pannala, R.R. Dehoff, S.S. Babu, The metallurgy and processing science of metal additive manufacturing, Int. Mater. Rev. 61(5) (2016) 315-360.

[2] T. DebRoy, H.L. Wei, J.S. Zuback, T. Mukherjee, J.W. Elmer, J.O. Milewski, A.M. Beese, A. Wilson-Heid, A. De, W. Zhang, Additive manufacturing of metallic components – Process, structure and properties, Prog. Mater. Sci. 92 (2018) 112-224.

[3] W.S. Miller, L. Zhuang, J. Bottema, A.J. Wittebrood, P. De Smet, A. Haszler, A. Vieregge, Recent development in aluminium alloys for the automotive industry, Mater. Sci. Eng., A 280(1) (2000) 37-49.

[4] R.A. Michi, A. Plotkowski, A. Shyam, R.R. Dehoff, S.S. Babu, Towards high-temperature applications of aluminium alloys enabled by additive manufacturing, Int. Mater. Rev. (2021) 1-48.

[5] N.T. Aboulkhair, M. Simonelli, L. Parry, I. Ashcroft, C. Tuck, R. Hague, 3D printing of Aluminium alloys: Additive Manufacturing of Aluminium alloys using selective laser melting, Prog. Mater. Sci. 106 (2019) 100578.

[6] A.I. Mertens, J. Delahaye, J. Lecomte-Beckers, Fusion-Based Additive Manufacturing for Processing Aluminum Alloys: State-of-the-Art and Challenges, Adv. Eng. Mater. 19(8) (2017) 1700003.

[7] E.O. Olakanmi, R.F. Cochrane, K.W. Dalgarno, A review on selective laser sintering/melting (SLS/SLM) of aluminium alloy powders: Processing, microstructure, and properties, Prog. Mater. Sci. 74 (2015) 401-477.

[8] J. Zhang, B. Song, Q. Wei, D. Bourell, Y. Shi, A review of selective laser melting of aluminum alloys: Processing, microstructure, property and developing trends, J. Mater. Sci. Technol. 35(2) (2019) 270-284.

[9] A. Aversa, G. Marchese, A. Saboori, E. Bassini, D. Manfredi, S. Biamino, D. Ugues, P. Fino, M. Lombardi, New Aluminum Alloys Specifically Designed for Laser Powder Bed Fusion: A Review, Materials (Basel) 12(7) (2019) 1007.

[10] R.S. Mishra, S. Thapliyal, Design approaches for printability-performance synergy in Al alloys for laser-powder bed additive manufacturing, Mater. Des. 204 (2021) 109640.

[11] J.H. Martin, B.D. Yahata, J.M. Hundley, J.A. Mayer, T.A. Schaedler, T.M. Pollock, 3D printing of high-strength aluminium alloys, Nature 549(7672) (2017) 365-369.

[12] S. Griffiths, J.R. Croteau, M.D. Rossell, R. Erni, A. De Luca, N.Q. Vo, D.C. Dunand, C. Leinenbach, Coarsening- and creep resistance of precipitation-strengthened Al–Mg–Zr alloys processed by selective laser melting, Acta Mater. 188 (2020) 192-202.

[13] S. Griffiths, M.D. Rossell, J. Croteau, N.Q. Vo, D.C. Dunand, C. Leinenbach, Effect of laser rescanning on the grain microstructure of a selective laser melted Al-Mg-Zr alloy, Mater. Charact. 143 (2018) 34-42.

[14] J.A. Glerum, C. Kenel, T. Sun, D.C. Dunand, Synthesis of precipitation-strengthened Al-Sc, Al-Zr and Al-Sc-Zr alloys via selective laser melting of elemental powder blends, Addit. Manuf. 36 (2020) 101461.

[15] Q. Jia, P. Rometsch, P. Kürnsteiner, Q. Chao, A. Huang, M. Weyland, L. Bourgeois, X. Wu, Selective laser melting of a high strength AlMnSc alloy: Alloy design and strengthening mechanisms, Acta Mater. 171 (2019) 108-118.

[16] A.B. Spierings, K. Dawson, T. Heeling, P.J. Uggowitzer, R. Schäublin, F. Palm, K. Wegener, Microstructural features of Sc- and Zr-modified Al-Mg alloys processed by selective laser melting, Mater. Des. 115 (2017) 52-63.

[17] M. Opprecht, J.-P. Garandet, G. Roux, C. Flament, M. Soulier, A solution to the hot cracking problem for aluminium alloys manufactured by laser beam melting, Acta Mater. 197 (2020) 40-53.

[18] X. Liu, Y. Liu, Z. Zhou, K. Wang, Q. Zhan, X. Xiao, Grain refinement and crack inhibition of selective laser melted AA2024 aluminum alloy via inoculation with TiC–TiH2, Mater. Sci. Eng., A 813 (2021) 141171.

[19] Q. Tan, J. Zhang, Q. Sun, Z. Fan, G. Li, Y. Yin, Y. Liu, M.-X. Zhang, Inoculation treatment of an additively manufactured 2024 aluminium alloy with titanium nanoparticles, Acta Mater. 196 (2020) 1-16.

[20] P. Mair, V.S. Goettgens, T. Rainer, N. Weinberger, I. Letofsky-Papst, S. Mitsche, G. Leichtfried, Laser powder bed fusion of nano-CaB6 decorated 2024 aluminum alloy, J. Alloys Compd. 863 (2021) 158714.

[21] L. Zhou, H. Hyer, J. Chang, A. Mehta, T. Huynh, Y. Yang, Y. Sohn, Microstructure, mechanical performance, and corrosion behavior of additively manufactured aluminum alloy 5083 with 0.7 and 1.0 wt% Zr addition, Mater. Sci. Eng., A 823 (2021) 141679.

[22] M.L. Montero-Sistiaga, R. Mertens, B. Vrancken, X. Wang, B. Van Hooreweder, J.-P. Kruth, J. Van Humbeeck, Changing the alloy composition of Al7075 for better processability by selective laser melting, J. Mater. Process. Technol. 238 (2016) 437-445.

[23] S.Y. Zhou, Y. Su, H. Wang, J. Enz, T. Ebel, M. Yan, Selective laser melting additive manufacturing of 7xxx series Al-Zn-Mg-Cu alloy: Cracking elimination by co-incorporation of Si and TiB2, Addit. Manuf. 36 (2020) 101458.

[24] Y. Otani, S. Sasaki, Effects of the addition of silicon to 7075 aluminum alloy on microstructure, mechanical properties, and selective laser melting processability, Mater. Sci. Eng., A 777 (2020) 139079.

[25] F. Czerwinski, Cerium in aluminum alloys, J. Mater. Sci. 55(1) (2020) 24-72.

[26] F. Czerwinski, Thermal Stability of Aluminum Alloys, Materials 13(15) (2020) 3441.

[27] Y. Liu, R.A. Michi, D.C. Dunand, Cast near-eutectic Al-12.5 wt.% Ce alloy with high coarsening and creep resistance, Mater. Sci. Eng., A 767 (2019) 138440.

[28] D.S. Ng, D.C. Dunand, Aging- and creep-resistance of a cast hypoeutectic Al-6.9Ce-9.3Mg (wt.%) alloy, Mater. Sci. Eng., A 786 (2020) 139398.

[29] A. Plotkowski, O. Rios, N. Sridharan, Z. Sims, K. Unocic, R.T. Ott, R.R. Dehoff, S.S. Babu, Evaluation of an Al-Ce alloy for laser additive manufacturing, Acta Mater. 126 (2017) 507-519.

[30] A. Plotkowski, K. Sisco, S. Bahl, A. Shyam, Y. Yang, L. Allard, P. Nandwana, A.M. Rossy, R.R. Dehoff, Microstructure and properties of a high temperature Al–Ce–Mn alloy produced by additive manufacturing, Acta Mater. 196 (2020) 595-608.

[31] Y. Yang, S. Bahl, K. Sisco, M. Lance, D. Shin, A. Shyam, A. Plotkowski, R.R. Dehoff, Primary solidification of ternary compounds in Al-rich Al–Ce–Mn alloys, J. Alloys Compd. 844 (2020) 156048.

[32] L. Zhou, T. Huynh, S. Park, H. Hyer, A. Mehta, S. Song, Y. Bai, B. McWilliams, K. Cho, Y. Sohn, Laser powder bed fusion of Al–10 wt% Ce alloys: microstructure and tensile property, J. Mater. Sci. 55(29) (2020) 14611-14625.

[33] Z.C. Sims, O.R. Rios, D. Weiss, P.E.A. Turchi, A. Perron, J.R.I. Lee, T.T. Li, J.A. Hammons, M. Bagge-Hansen, T.M. Willey, K. An, Y. Chen, A.H. King, S.K. McCall, High performance aluminum–cerium alloys for high-temperature applications, Materials Horizons 4(6) (2017) 1070-1078.

[34] F. Czerwinski, A search for the eutectic system of high-temperature cast aluminium alloys, Mater. Sci. Technol. (2021) 1-10.

[35] F. Czerwinski, Thermal stability of aluminum–cerium binary alloys containing the Al–Al11Ce3 eutectic, Mater. Sci. Eng., A 809 (2021) 140973.

[36] K. Sisco, A. Plotkowski, Y. Yang, D. Leonard, B. Stump, P. Nandwana, R.R. Dehoff, S.S. Babu, Microstructure and properties of additively manufactured Al–Ce–Mg alloys, Sci. Rep. 11(1) (2021) 6953.

[37] D.R. Manca, A.Y. Churyumov, A.V. Pozdniakov, A.S. Prosviryakov, D.K. Ryabov, A.Y. Krokhin, V.A. Korolev, D.K. Daubarayte, Microstructure and Properties of Novel Heat Resistant Al–Ce–Cu Alloy for Additive Manufacturing, Met. Mater. Int. 25(3) (2019) 633-640.

[38] N.E. Uzan, R. Shneck, O. Yeheskel, N. Frage, High-temperature mechanical properties of AlSi10Mg specimens fabricated by additive manufacturing using selective laser melting technologies (AM-SLM), Addit. Manuf. 24 (2018) 257-263.

[39] Z. Wang, X. Lin, N. Kang, Y. Hu, J. Chen, W. Huang, Strength-ductility synergy of selective laser melted Al-Mg-Sc-Zr alloy with a heterogeneous grain structure, Addit. Manuf. 34 (2020) 101260.

[40] J.R. Croteau, S. Griffiths, M.D. Rossell, C. Leinenbach, C. Kenel, V. Jansen, D.N. Seidman, D.C. Dunand, N.Q. Vo, Microstructure and mechanical properties of Al-Mg-Zr alloys processed by selective laser melting, Acta Mater. 153 (2018) 35-44.

[41] K.E. Knipling, D.C. Dunand, D.N. Seidman, Criteria for developing castable, creep-resistant aluminum-based alloys–A review, Zeitschrift für METALLKUNDE 97(3) (2006) 246-265.

[42] A.S. Sabau, S. Mirmiran, C. Glaspie, S.M. Li, D. Apelian, A. Shyam, J.A. Haynes, A.F. Rodriguez, Hot-Tearing Assessment of Multicomponent Nongrain-Refined Al-Cu Alloys for Permanent Mold Castings Based on Load Measurements in a Constrained Mold, Metall. Mater. Trans. B 49(3) (2018) 1267-1287.

[43] A. Shyam, A. Plotkowski, S. Bahl, K. Sisco, L.F. Allard, Y. Yang, J.A. Haynes, R.R. Dehoff, An additively manufactured AlCuMnZr alloy microstructure and tensile mechanical properties, Materialia 12 (2020) 100758.

[44] S. Bahl, A. Plotkowski, K. Sisco, D.N. Leonard, L.F. Allard, R.A. Michi, J.D. Poplawsky, R. Dehoff, A. Shyam, Elevated temperature ductility dip in an additively manufactured Al-Cu-Ce alloy, Acta Mater. (2021) 117285.

[45] B. Gault, M.P. Moody, J.M. Cairney, S.P. Ringer, Atom probe microscopy, Springer Science & Business Media2012.

[46] B. Gault, M.P. Moody, J.M. Cairney, S.P. Ringer, Atom probe crystallography, Mater. Today 15(9) (2012) 378-386.

[47] R.A. Michi, J. Perrin Toinin, A.R. Farkoosh, D.N. Seidman, D.C. Dunand, Effects of Zn and Cr additions on precipitation and creep behavior of a dilute Al–Zr–Er–Si alloy, Acta Mater. 181 (2019) 249-261.

[48] M. Hellenbrandt, The Inorganic Crystal Structure Database (ICSD)—Present and Future, Crystallography Reviews 10(1) (2004) 17-22.

[49] L. Kaufman, H. Bernstein, Computer calculation of phase diagrams With special reference to refractory metals, Academic Press Inc, United States, 1970.

[50] H. Bo, S. Jin, L.G. Zhang, X.M. Chen, H.M. Chen, L.B. Liu, F. Zheng, Z.P. Jin, Thermodynamic assessment of Al–Ce–Cu system, J. Alloys Compd. 484(1) (2009) 286-295.

[51] N.A. Belov, A.V. Khvan, The ternary Al–Ce–Cu phase diagram in the aluminum-rich corner, Acta Mater. 55(16) (2007) 5473-5482.

[52] A.T. Dinsdale, SGTE data for pure elements, Calphad 15(4) (1991) 317-425.

[53] S. Kou, A criterion for cracking during solidification, Acta Mater. 88 (2015) 366-374.

[54] O.S. Zarechnyuk, P.I. Kripyakevich, I.F. Kolobnev, E.E. Cherkashin, The quaternary compound Ce3 Mn Cu8 Al24 and its crystal structure, Izvestiya Akademii Nauk SSSR, Neorganicheskie Materialy 3 (1967) 182 - 183.

[55] APWorks, Material Data Sheet- Scalmalloy, https://www.apworks.de/scalmalloy

[56] J.A. Dantzig, M. Rappaz, Solidification: -Revised & Expanded, EPFL press2016.

[57] W. Kurz, D.J. Fisher, Dendrite growth in eutectic alloys: the coupled zone, International Metals Reviews 24(1) (1979) 177-204.

[58] S. Fukumoto, W. Kurz, Solidification Phase and Microstructure Selection Maps for Fe-Cr-Ni Alloys, ISIJ Int. 39(12) (1999) 1270-1279.

[59] S.S. Babu, J.W. Elmer, J.M. Vitek, S.A. David, Time-resolved X-ray diffraction investigation of primary weld solidification in Fe-C-Al-Mn steel welds, Acta Mater. 50(19) (2002) 4763-4781.

[60] P. Mohammadpour, A. Plotkowski, A.B. Phillion, Revisiting solidification microstructure selection maps in the frame of additive manufacturing, Addit. Manuf. 31 (2020) 100936.

[61] Q. Jia, F. Zhang, P. Rometsch, J. Li, J. Mata, M. Weyland, L. Bourgeois, M. Sui, X. Wu, Precipitation kinetics, microstructure evolution and mechanical behavior of a developed Al–Mn–Sc alloy fabricated by selective laser melting, Acta Mater. 193 (2020) 239-251.

[62] L. Zhou, H. Pan, H. Hyer, S. Park, Y. Bai, B. McWilliams, K. Cho, Y. Sohn, Microstructure and tensile property of a novel AlZnMgScZr alloy additively manufactured by gas atomization and laser powder bed fusion, Scripta Mater. 158 (2019) 24-28.

[63] T. Philippe, P.W. Voorhees, Ostwald ripening in multicomponent alloys, Acta Mater. 61(11) (2013) 4237-4244.

[64] A. De Luca, D.C. Dunand, D.N. Seidman, Microstructure and mechanical properties of a precipitation-strengthened Al-Zr-Sc-Er-Si alloy with a very small Sc content, Acta Mater. 144 (2018) 80-91.

[65] P. Okle, J.D. Lin, T. Zhu, D.C. Dunand, D.N. Seidman, Effect of micro-additions of Ge, In or Sn on precipitation in dilute Al-Sc-Zr alloys, Mater. Sci. Eng., A 739 (2019) 427-436.

[66] P. Pandey, S.K. Makineni, B. Gault, K. Chattopadhyay, On the origin of a remarkable increase in the strength and stability of an Al rich Al-Ni eutectic alloy by Zr addition, Acta Mater. 170 (2019) 205-217.

[67] D. Porter, K. Easterling, Phase Transformations in Metals and Alloys (Revised Reprint), 3rd Edition ed., CRC Press, Boca Raton, 2009.

[68] J.F. Nie, B.C. Muddle, Strengthening of an Al–Cu–Sn alloy by deformation-resistant precipitate plates, Acta Mater. 56(14) (2008) 3490-3501.

[69] N. Hansen, Hall–Petch relation and boundary strengthening, Scripta Mater. 51(8) (2004) 801-806.

[70] G. Requena, G. Garcés, Z. Asghar, E. Marks, P. Staron, P. Cloetens, The Effect of the Connectivity of Rigid Phases on Strength of Al-Si Alloys, Adv. Eng. Mater. 13(8) (2011) 674-684.

[71] D.-K. Kim, W. Woo, J.-H. Hwang, K. An, S.-H. Choi, Stress partitioning behavior of an AlSi10Mg alloy produced by selective laser melting during tensile deformation using in situ neutron diffraction, J. Alloys Compd. 686 (2016) 281-286.

[72] S. Bahl, S. Suwas, T. Ungàr, K. Chatterjee, Elucidating microstructural evolution and strengthening mechanisms in nanocrystalline surface induced by surface mechanical attrition treatment of stainless steel, Acta Mater. 122 (2017) 138-151.

[73] S. Bahl, L. Xiong, L.F. Allard, R.A. Michi, J.D. Poplawsky, A.C. Chuang, D. Singh, T.R. Watkins, D. Shin, J.A. Haynes, A. Shyam, Aging behavior and strengthening mechanisms of coarsening resistant metastable θ' precipitates in an Al–Cu alloy, Mater. Des. 198 (2021) 109378.

[74] K.E. Knipling, R.A. Karnesky, C.P. Lee, D.C. Dunand, D.N. Seidman, Precipitation evolution in Al–0.1Sc, Al–0.1Zr and Al–0.1Sc–0.1Zr (at.%) alloys during isochronal aging, Acta Mater. 58(15) (2010) 5184-5195.

[75] D.N. Seidman, E.A. Marquis, D.C. Dunand, Precipitation strengthening at ambient and elevated temperatures of heat-treatable Al(Sc) alloys, Acta Mater. 50(16) (2002) 4021-4035.

[76] A.J. Ardell, Precipitation hardening, Metall. Trans. A 16(12) (1985) 2131-2165.

[77] G. Ghosh, S. Vaynman, M. Asta, M.E. Fine, Stability and elastic properties of L12-(Al,Cu)3(Ti,Zr) phases: Ab initio calculations and experiments, Intermetallics 15(1) (2007) 44-54.

[78] W. Lefebvre, N. Masquelier, J. Houard, R. Patte, H. Zapolsky, Tracking the path of dislocations across ordered Al3Zr nano-precipitates in three dimensions, Scripta Mater. 70 (2014) 43-46.

[79] C.S. Tiwary, P. Pandey, S. Sarkar, R. Das, S. Samal, K. Biswas, K. Chattopadhyay, Five decades of research on the development of eutectic as engineering materials, Prog. Mater. Sci. (2021) 100793.

[80] N. Takata, H. Kodaira, K. Sekizawa, A. Suzuki, M. Kobashi, Change in microstructure of selectively laser melted AlSi10Mg alloy with heat treatments, Mater. Sci. Eng., A 704 (2017) 218-228.

[81] X. Qi, N. Takata, A. Suzuki, M. Kobashi, M. Kato, Managing both high strength and thermal conductivity of a laser powder bed fused Al–2.5Fe binary alloy: Effect of annealing on microstructure, Mater. Sci. Eng., A 805 (2021) 140591.

[82] P. Krakhmalev, A.M. Vilardell, N. Takata, 13 - Structural integrity I: static mechanical properties, in: I. Yadroitsev, I. Yadroitsava, A. du Plessis, E. MacDonald (Eds.), Fundamentals of Laser Powder Bed Fusion of Metals, Elsevier2021, pp. 349-376.